



FRONTIER ARTICLE

10.1029/2018GL079162

Special Section:

Impact of the Sept. 10, 2017,
solar event on Mars

Key Points:

- An X8.2 solar flare, ICME, and associated solar energetic particles impacted Mars beginning on 10 September 2017
- This was the largest event observed at Mars simultaneously in orbit by the current flotilla of spacecraft and at the surface by a lander
- Observations included the solar event, significant effects on the upper atmosphere and ionosphere, and influence on escape of gas to space

Correspondence to:

C. O. Lee,
clee@ssl.berkeley.edu

Citation:

Lee, C. O., Jakosky, B. M., Luhmann, J. G., Brain, D. A., Mays, M. L., Hassler, D. M., et al. (2018). Observations and impacts of the 10 September 2017 solar events at Mars: An overview and synthesis of the initial results. *Geophysical Research Letters*, 45. <https://doi.org/10.1029/2018GL079162>

Received 9 JUN 2018

Accepted 27 JUL 2018

Accepted article online 6 AUG 2018

Observations and Impacts of the 10 September 2017 Solar Events at Mars: An Overview and Synthesis of the Initial Results

C. O. Lee¹ , B. M. Jakosky² , J. G. Luhmann¹ , D. A. Brain² , M. L. Mays³ , D. M. Hassler⁴ , M. Holmström⁵ , D. E. Larson¹ , D. L. Mitchell¹ , C. Mazelle⁶ , and J. S. Halekas⁷ 

¹Space Sciences Laboratory, University of California, Berkeley, CA, USA, ²Laboratory for Atmospheric and Space Physics, University of Colorado Boulder, Boulder, Colorado, USA, ³CCMC/NASA Goddard Space Flight Center, Greenbelt, MD, USA, ⁴Space Science and Engineering Division, Southwest Research Institute, Boulder, CO, USA, ⁵Swedish Institute of Space Physics, Kiruna, Sweden, ⁶Institut de Recherche en Astrophysique et Planétologie, Université de Toulouse, CNRS, UPS, CNES, Toulouse, France, ⁷Department of Physics and Astronomy, University of Iowa, Iowa City, IA, USA

Abstract On 10 September 2017, some of the strongest solar activity occurred in association with active region 12673 (AR2673), including an X-class solar flare and a fast coronal mass ejection. Although AR2673 was not centrally facing Mars, the activity impacted the local space weather conditions at Mars. We give an overview of observations obtained from the Mars Atmosphere and Volatile Evolution, Mars Science Laboratory, and Mars Express missions. Numerical results from the Wang-Sheeley-Argue (WSA)-Enlil-cone model together with Earth/L1 and STEREO-A observations are also presented to provide some heliospheric context. We discuss the initial results on the space weather impacts at Mars, which include heating of the upper atmosphere by solar flare emissions, flare-related enhancements of ion and neutral densities, solar energetic particles impacting the atmosphere and surface, bright emissions of a diffuse (global) aurora, deeply penetrating interplanetary magnetic fields over the Martian dayside, and enhanced atmospheric escape rates.

Plain Language Summary When an X8.2 class flare and a fast and wide coronal mass ejection (CME) erupted from active region 12673 (AR2673) on 10 September 2017, the space weather impact was widespread and observed at multiple locations including Earth, Mars, and STEREO-A. The collection of papers in this GRL volume focuses on the observations and impacts at Mars triggered by these solar eruptive events. The space weather effects at Mars were simultaneously observed by instruments across several Mars missions, including Mars Atmosphere and Volatile Evolution, Mars Science Laboratory, Mars Express, Mars Odyssey, and also Trace Gas Orbiter. These September events began with two large M-class flares and one X-class flare observed at Mars together with CME activity seen in the solar coronagraphs at Earth. High fluxes of solar energetic particles associated with the flare and CME eruption were also detected. In this introduction, we provide an overview of the solar and heliospheric observations of the 10 September 2017 solar activity to provide context for the initial results on the space weather impacts. We present our summary and synthesis in this article.

1. Introduction

When an X8.2 class flare and a fast and wide coronal mass ejection (CME) erupted from active region 12673 (hereafter, AR2673) on 10 September 2017, the space weather impact was widespread and observed at multiple locations including Earth, Mars, and STEREO-A (hereafter, STA; Kaiser, 2005). The collection of papers in this GRL volume focuses on the observations and impacts at Mars triggered by these solar eruptive events. The space weather effects at Mars were simultaneously observed by instruments across several Mars missions, including Mars Atmosphere and Volatile Evolution (MAVEN), Mars Science Laboratory (MSL), Mars Express (MEX), Mars Odyssey (MO), and also Trace Gas Orbiter (TGO). A collection of papers that discusses the observations and impacts at Earth may be found in the *Space Weather Journal* (2018).

These September events began with two large M-class flares and one X-class flare observed at Mars (Chamberlin et al., 2018) together with CME activity seen in the solar coronagraphs at Earth and STA. High

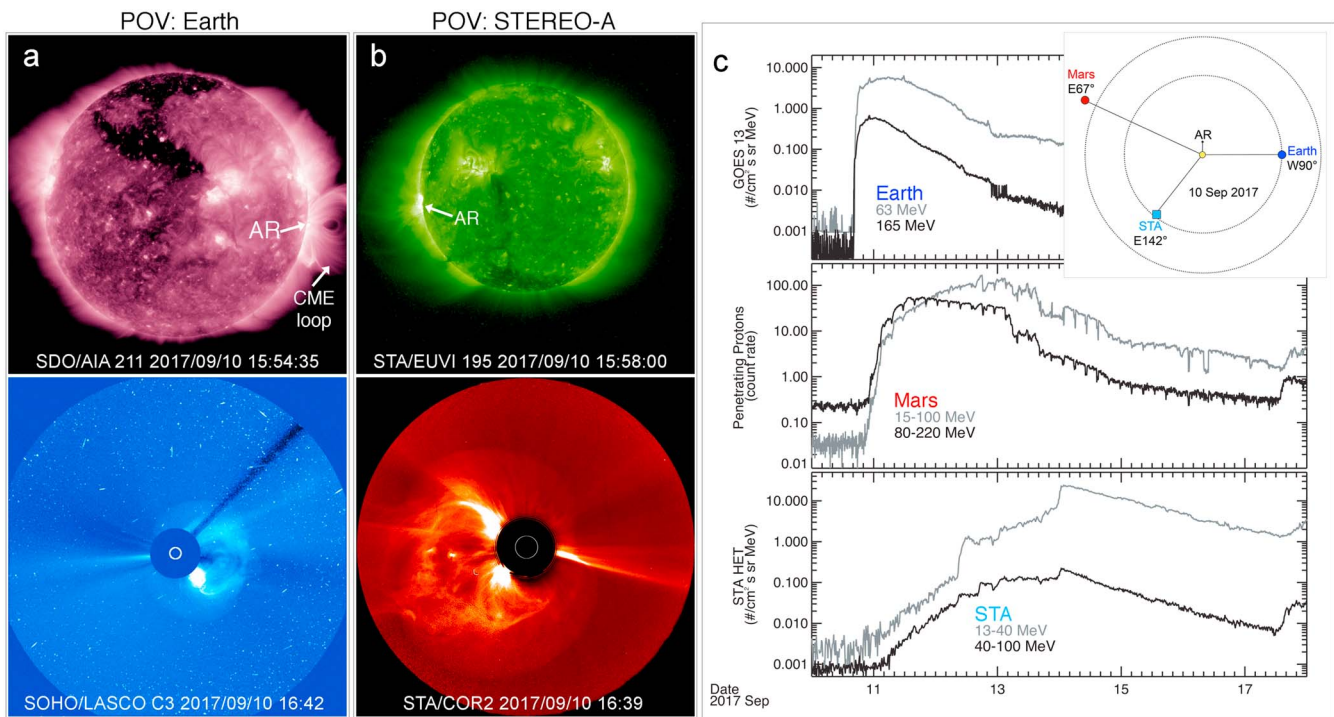


Figure 1. (a) Top panel shows the CME eruption site near AR2673 on the solar disk by SDO/AIA. Bottom panel shows the CME structure at 16:24 UT by SOHO/LASCO C3. (b) Top panel shows the eruption site from STA/EUVI. Bottom panel shows CME structure at 16:24 UT by STA/COR2. (c) Higher energy (dark gray) and lower energy (light gray) SEP proton observations by GOES-13 at Earth (top panel), MAVEN/SEP at Mars (middle panel), and STA/HET (bottom panel). The inset shows the Earth, Mars, and STA heliolongitude locations with respect to the AR2673 location on the Sun, as labeled.

fluxes of solar energetic particles (SEPs) associated with the flare and CME eruption were also detected (e.g., see Luhmann et al., 2018). In section 2 we provide an overview of the solar and heliospheric observations of the 10 September 2017 solar activity to provide context for sections 3–6 where we present and synthesize the initial results presented in this GRL volume on the space weather impacts at Mars. Numerical results for the event period (WSA-Enlil-cone event simulation made by special request through the NASA Community Coordinated Modeling Center; run name “Leila_Mays_120817_SH_9.”) from the Wang-Sheeley-Argue (WSA)-Enlil coupled solar corona-solar wind model (hereafter, WSA-Enlil; Arge et al., 2004; Odstrcil, 2003) are used to illustrate the global context of the solar and heliospheric sources of the space weather conditions observed at Mars during this event period.

2. Solar Eruptive Activity on 10 September 2017

The strong solar activity began with the eruption of the X8.2 class flare from AR2673 on 10 September 2017. The flare was initially observed at Earth by the NOAA Geostationary Operational Environmental Satellites (GOES; Aschwanden, 1994) X-ray flux instrument in the 0.1- to 0.8-nm channel for solar soft X-rays. The event start time was ~15:35 UT and peaked at ~16:06 UT before slowly returning to the background levels at ~16:31 UT (the start and end times are based on the full-width, half maximum values). Solar images taken near Earth from the Solar Dynamics Observatory (SDO; Pesnell et al., 2012) Atmospheric Imaging Assembly (AIA; Lemen et al., 2012), such as Figure 1a (top panel), show that AR2673 was located around the western limb of the solar disk (~W90°, where 0° longitude is located at the center of the solar disk) when the flare erupted. At the STA location, AR2673 was seen near the eastern limb (~E90°), as shown in Figure 1b (top panel) from the STA Extreme Ultraviolet Imager (EUVI).

Although there is no solar imager present at Mars, the Extreme Ultraviolet Monitor (EUVM; Eparvier et al., 2015) on board MAVEN did observe an increase in solar irradiance during the flare (Chamberlin et al., 2018). Located ~0.66 AU further away, EUVM detected the flare ~5.5 min after GOES. From the Mars vantage point, AR2673 would have been visible on the solar disk at ~E67°. The inset of Figure 1c illustrates the relative locations of Earth, Mars, and STA with respect to the solar longitude location of AR2673 during the event period.

MAVEN/EUVM can measure the solar emissions from the hot solar corona in the wavelength range of 0.1- to 7-nm (science channel B, hereafter EUVM-B), which responds to solar flares in a manner similar to the GOES X-ray flux instrument. MAVEN/EUVM also measures the hydrogen Lyman- α emission at 121.6 nm (science channel C), which responds to the increase in solar EUV and the more impulsive (earlier) phase of the solar flare. Figure 3a, which will be discussed in detail in section 3, shows EUVM-B soft X-ray irradiance observations of the X-class flare with a peak flare time at 15:40:30 UT (dashed magenta line labeled “F”). Also, the MAVEN/SEP instrument (Larson et al., 2015) detected the solar flare hard X-rays in its “thick” detector at \sim 15:54 UT, with a similar peak time of 16:02 UT as the Lyman- α emission (not shown).

The solar activity around AR2673 continued with the eruption of a fast and wide CME. The SDO/AIA 211 image taken at 15:54:35 UT shows a bright CME magnetic field loop around AR2673 (Figure 1a, top panel). The CME was later observed by the Solar and Heliospheric Observatory (SOHO) Large Angle and Spectrometric Coronagraph (LASCO; Brueckner et al., 1995) and the STA Sun Earth Connection Coronal and Heliospheric Investigation (SECCHI) COR2 coronagraph. The leading edge of the CME entered the LASCO/C2 FOV ($1.5\text{--}6 R_{\odot}$) at 16:00 UT and the LASCO/C3 FOV ($3.8\text{--}32 R_{\odot}$) between 16:06 UT to 16:18 UT. Based on these observations, an initial linear speed of \sim 3,300 km/s was estimated (see the SOHO Halo CME alert at <https://umbra.nascom.nasa.gov/lasco/observations/halo/2017/170910/>). The bottom panels of Figures 1a and 1b show a bright and wide CME from the vantage points of Earth (LASCO/C3) and STA (SECCHI/COR2), respectively.

High-energy SEP protons associated with this fast CME were observed at Earth and STA as well as at Mars. Figure 1c (top to bottom) shows the SEP proton measurements by GOES-13, MAVEN/SEP, and the STA High Energy Telescope (HET; von Rosenvinge et al., 2008). Because of the western location of AR2673 with respect to the Sun-Earth line, GOES-13 detected the prompt arrival of SEP protons (at \sim 16:30 UT on 10 September 2017 for the 165-MeV energy channel shown) due to the apparent magnetic field line connection of Earth to the CME-driven shock source near the Sun. Meanwhile, AR2673 was located at $E67^{\circ}$ with respect to the Sun-Mars line and thus MAVEN/SEP detected a later arrival of SEP protons (at \sim 22:00 UT on 10 September 2017 for the 80- to 220-MeV energy channel shown) when the CME shock was further away from the Sun and magnetically connected to Mars (for example, see Figure 6d in Luhmann et al., 2018). STA/HET detected SEP protons even later (at \sim 06:00 UT on 11 September 2017 for the 60- to 100-MeV energy channel shown) when the CME shock had travelled further outward to magnetically connect with STA (for example, see Figure 6b in Luhmann et al., 2018).

The WSA-Enlil simulation snapshots (Figure 2) show the evolution of the ecliptic solar wind speeds and CME structure over a period of several days. Figures 2a–2b show the parameterized CME clouds for two slower CMEs that erupted on 9 September 2017 and merged together (CME1+2) and the faster CME that erupted on 10 September 2017 (CME3). Since CME3 is moving faster and propagating in the same radial direction as CME1+2, CME3 interacts with CME1+2 from behind to become a single, merged CME structure (panel 2c), as described by Guo, Dumbovic et al. (2018). Panels 2d–2f show the modeling results of the merged CME structure encountering Venus and STEREO-B before reaching Mars at \sim 00:00 UT on 13 September 2017, \sim 60 hours after the CME eruption. In Section 5 we will show that the modeled arrival time of the CME at Mars matches well with the in situ observations of the event.

For this article, we use the WSA-Enlil simulation results as a tool toward interpreting the solar wind and CME observations at Mars. The simulation details are described in the Space Weather paper by Luhmann et al. (2018) that uses the Enlil results to model the associated SEP observations for the July and September 2017 event periods. In general, the limitations of WSA-Enlil to accurately model the CME event include the uncertainties in the input solar photospheric field maps that are used to drive the background solar wind simulations, the use of a geometrical cone shape to approximate the shape of a CME, the accuracy of the CME parameterization (injection direction, time, and size), and the lack of the ejecta field description in Enlil, which affects the CME expansion during the propagation (Lee et al., 2013, 2015; Mays et al., 2015). Nevertheless it is found that the simulation often produces a good first-order approximation to the heliospheric conditions associated with real CMEs, including time series of plasma velocities and ICME shock arrival times.

3. Heating of Mars' Atmosphere by the Flare Photons

The X8.2 class flare on 10 September 2017 was the largest known event of Solar Cycle 24 to impact Mars and the largest event observed to date by MAVEN/EUVM. While previous studies have reported the Mars

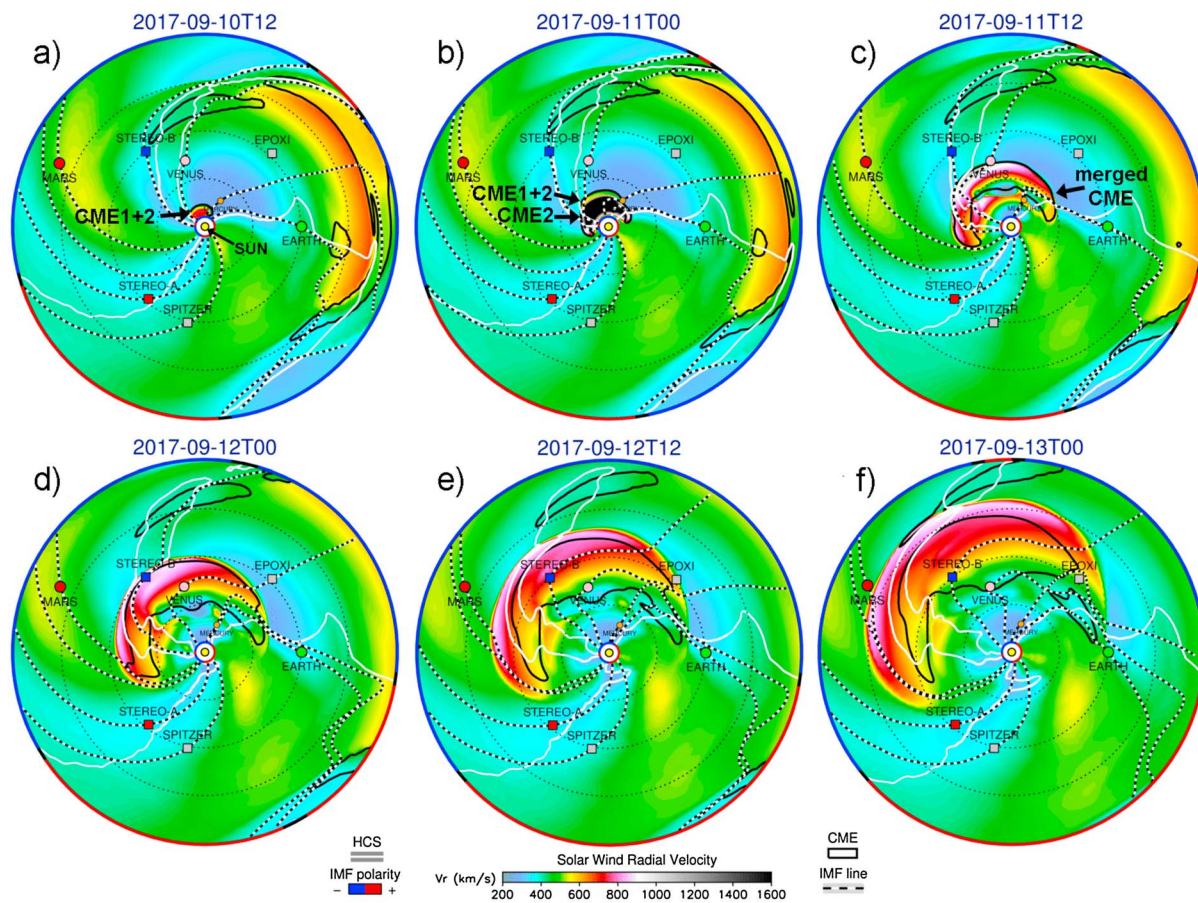


Figure 2. WSA-Enlil simulation snapshots showing the eruption and evolution of the 10 September 2017 CME structure, from 21.5 R_{\odot} to Mars (red circle). (a) Two CMEs that erupted on 9 September 2017 CME appear in the simulation frame as a merged structure (CME1+2). (b) The 10 September 2017 CME (CME3) approaches CME1+2 from behind. (c–f) CME1+2 and CME3 propagate toward Mars as a merged structure. The colors shown are the modeled radial solar wind speeds in the ecliptic plane.

ionosphere (Gurnett et al., 2005) and thermosphere (Thiemann et al., 2015) responses to solar flares for individual events using separate spacecraft observations, multiple instruments onboard MAVEN simultaneously observed both the thermosphere and ionosphere response to the 10 September 2017 flare. Although the bulk ionospheric plasma enhancement is expected to be brief, following the time profile of the flare (Lollo et al., 2012; Mendillo et al., 1974), the thermosphere is seen to respond more slowly.

At ~ 170 km in the thermosphere, Jain et al. (2018) report a temperature increase of ~ 70 K during the flare, based on airglow measurements from the MAVEN Imaging UltraViolet Spectrograph (IUVS) instrument. They also found that the flare heating was more pronounced at the low-to-mid latitudes of Mars. One possible explanation is that upper atmosphere dynamics prevented the heating from the flare near the subsolar point to dissipate to higher latitudes. An example of the MAVEN/IUVS temperature time profile is shown in Figure 3k to illustrate the timing of the thermospheric response with the solar irradiance enhancement (Figure 3a).

Elrod et al. (2018) investigated the flare emission response of the upper atmospheric neutral species (Ar, CO_2 , CO, O and N_2) observed in situ by the MAVEN Neutral Gas and Ion Spectrometer (NGIMS; Mahaffy et al., 2015) and found that the atmosphere heated on a timescale similar to the duration of the flare event. Specifically, they found that during one orbit of observations coincident with the flare event, there was a significant density and temperature enhancement in the Martian neutral exosphere above 195 km. By the following orbit (~ 4.5 hours later), the observed densities and temperatures were at the approximate pre-flare event values. An example of the Ar densities (color contours) for a given altitude is shown in Figure 3l. A comparison with the MAVEN/EUVM observations (Figure 3a) and IUVS thermospheric temperature (Figure 3k) shows that enhanced Ar densities are correlated with the increase of solar irradiance. Since Ar is an inert gas, changes in the Ar temperatures are a good indicator of temperature changes in the upper atmosphere. Elrod et al. (2018)

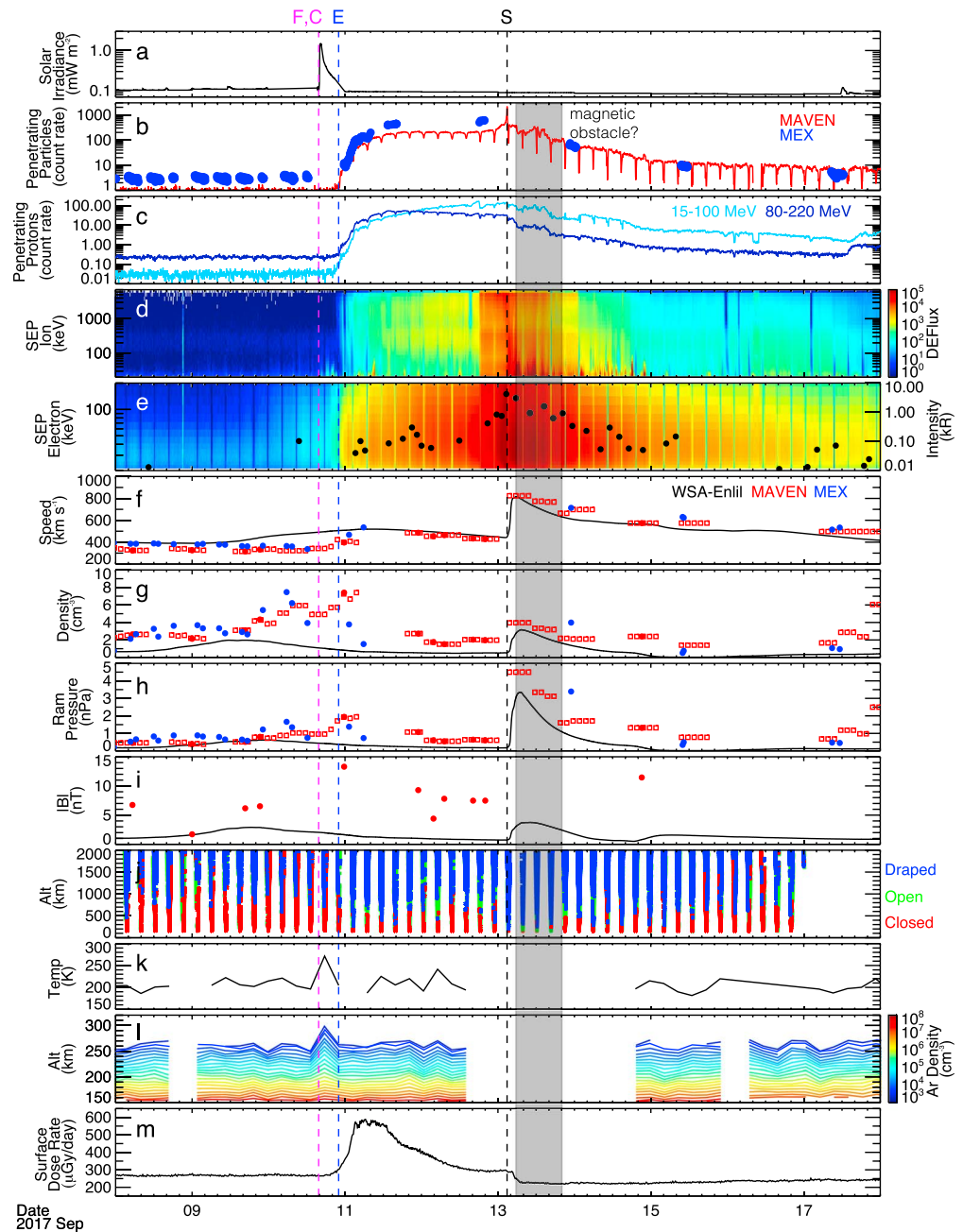


Figure 3. (a) MAVEN/EUVM solar irradiance in the 0.1–7 nm wavelength. (b) Penetrating background counts from MAVEN/SWEA (red) and MEX/ASPERS-3 IMA (blue). (c) 15–100 MeV (light blue) and 80–200 MeV (blue) SEP protons from MAVEN/SEP-FTO. (d–e) Differential energy fluxes of the MAVEN/SEP 20 keV to 6 MeV protons and 20 keV to 200 keV electrons. Overplotted are the IUVS auroral emission in kiloRayleighs (black circles). (f–i) Upstream solar wind speed, density, dynamic pressure, and IMF magnitude from MAVEN/SWIA and MAG (red filled circles), MEX/ASPERS-3 IMA (blue filled circles) and WSA-Enlil model (black line). Proxy solar wind values estimated from the MAVEN/SWIA penetrating proton measurements are also shown (red open squares). (j) Closed (red), open (green), and draped (blue) magnetic field topology for a given altitude. (k) Inferred thermospheric temperatures. (l) Color contours of Argon densities at a given height. (m) MSL/RAD surface radiation dose rate. Vertical lines mark the start of the flare (F), CME (C), SEP arrival (E), and ICME shock arrival (S). The vertical gray bar marks the ‘bite-out’ features seen in (b–c) due to the passage of the magnetic obstacle formed by the merged CMEs.

showed that the Ar density at a fixed altitude of 225 km increased by a factor of ~ 4 , and that the Ar temperature increased by ~ 90 K during the peak of the flare event. For all neutral species observed by NGIMS, the temperatures increased by ~ 100 K.

The first in situ observed flare response of the topside ionosphere thermal plasma temperature and composition is reported by Thiemann et al. (2018). Using observations from MAVEN/EUVIM, NGIMS, and the Langmuir Probe and Waves (LPW; Andersson et al., 2015) together with model calculations, they found that photon energy deposition was enhanced by $\sim 80\%$ at 110 km in the thermosphere, where most of the soft X-ray (SXR, 0.1–10 nm) photons deposited their energy, and the total photoionization rate increased by 500% at these altitudes. In the upper atmosphere, the total ionization rate increased by 20%. With the presence of more neutrals at high altitudes (due to an expanded neutral atmosphere), the MAVEN observations showed that the electron densities (n_e) and ion densities (for O_2^+ , CO_2^+ , and O^+) increased (see Figures 2 and 3 in Thiemann et al., 2018) while the electron heating was suppressed below ~ 220 km due to efficient electron cooling by CO_2 . Generally speaking, the observed changes in the ionosphere during the MAVEN observations obtained after the time of the flare peak are due to the expansion of the neutral atmosphere and altered neutral composition. In terms of compositional changes in the ionosphere, Thiemann et al. (2018) reported an increase in the production of O and thus an increase in the relative abundance of O at a fixed pressure, which has implications for photochemical escape (section 6).

Xu, Thiemann, et al. (2018) investigated the low-altitude ionospheric response to the X8.2 flare by SuperThermal Electron Transport (STET) model to simulate the photoelectron spectra and ion production rates and densities for periods before the flare, during the flare peak, and during the first MAVEN in situ observations of the period after the flare peak. A good agreement was found between the modeled photoelectron spectra and observations. In addition, the carbon Auger peak in the photoelectron spectra, produced by SXR photons ionizing the inner shell electrons and the sequential relaxation of electronically excited carbon ions by emitting electrons with a fixed energy ~ 250 eV, was repeatedly identified in the Martian ionosphere for the first time, due to the higher photoelectron fluxes during the flare interval. Based on their modeled O_2^+ and CO_2^+ densities for the three event intervals, they found that the enhancements due to the flare at a fixed altitude increased by a few tens of percent up to $\sim 1,500\%$.

4. SEPs at Mars

While the Martian atmosphere was responding to the energetic input from the X8.2 flare, a fast and wide CME had erupted in the general vicinity of the flare site. As the shock and the driver CME propagated toward and magnetically connected with Mars (e.g., Figures 2c–2f), the highest energy SEPs were detected by several instruments from MAVEN, MEX, and MSL Radiation Assessment Detector (RAD; Hassler et al., 2012).

4.1. SEPs in Near-Mars Space

As discussed in section 2, MAVEN/SEP detected 15- to 100-MeV and 80- to 220-MeV SEP protons several hours after the fast CME eruption. These high-energy SEPs penetrated through the MAVEN/SEP stack of silicon detectors called “foil,” “thick,” and “open” to trigger a Foil-Thick-Open (FTO) event type (see Figure 6 and related discussion in Larson et al., 2015). The direct measurements of incident energies and fluxes for SEPs detected in the FTO bins are currently unavailable since the instrument is optimized to measure 20-keV to 6-MeV protons (energies that are important for atmospheric escape). For the FTO observations reported here, the detected energy information together with the MAVEN/SEP instrument response matrices are used to constrain the incident energy range. Figure 3c shows the 15- to 100-MeV and 80- to 220-MeV SEP protons, with the vertical blue line (“E”) marking the SEP proton arrival time to Mars ($\sim 22:00$ UT on 10 September 2017). The peak detection of 80- to 220 MeV SEP protons occurred at $\sim 18:53$ UT on 11 September 2017 while peak detection for 15- to 100-MeV SEP protons occurred at $\sim 17:58$ UT on 12 September 2017.

A sharp rise was observed in the MAVEN energetic particle observations due to the ICME shock arrival at $\sim 02:52$ UT on 13 September 2017. This peak can be seen most clearly in the MAVEN Solar Wind Electron Analyzer (SWEA) penetrating counts in Figure 3b (vertical black line, “S”). The source for penetrating counts in SWEA are SEP protons with energies of a few tens of MeV (e.g., Figure 3c, cyan time series) and SEP electrons with energies of a few MeV penetrating the instrument housing. During this event MAVEN/SEP also measured fluxes for 20-keV to 6-MeV ions and 20-keV to 200-keV electrons (onset starting at $\sim 19:20$ UT on 10 September 2017 for > 100 -keV electrons) and detected a sharp peak in the fluxes as indicated by the darkest red color shown in Figures 3d and 3e. Such a peak in the particle observations is consistent with an energetic storm

particle (ESP) enhancement that occurs when an ICME shock passes the observer. Consistent with these observations, WSA-Enlil modeled the ICME impact to occur at Mars shortly after 00:00 UT on 13 September 2017 (Figure 2f). After the shock arrival the energetic particle enhancements slowly declined.

Penetrating background counts were also measured by the MEX/ASPERA-3 IMA instrument (Capalbo, 2010; Futaana et al., 2008), as shown in Figure 3b. The overall trend follows observations from MAVEN/SWEA and also MAVEN/SEP-FTO (Figure 3c). Ramstad et al. (2018) reported the first attempt to calibrate the IMA penetrating background counts with the MAVEN/SEP-FTO data. In doing so, they found that the IMA background counts are due to >1 MeV SEP electrons and >20 MeV protons. Given the high flux of SEPs measured by MAVEN/SEP during this event, they compared the counts for this event period to those over the entire MEX mission to date since 2004 and found that the September 2017 SEP event was the fourth strongest event detected at Mars since 2004.

4.2. SEPs in the Martian Upper Atmosphere

Harada et al. (2018) investigated the ionosphere response to SEPs using the nightside ionosphere observations from the MEX Mars Advanced Radar for Subsurface and Ionosphere Sounding (MARSIS) instrument (Gurnett et al., 2008) together with the MAVEN dayside observations. The MARSIS instrument in particular has been making ionospheric sounding measurements of the Martian topside ionosphere, which can be used to infer the vertical electron density profiles of the topside ionosphere. During the SEP event period, MARSIS detected ionospheric echoes with unusually high peak electron densities ($\sim 1\text{--}2 \times 10^4 \text{ cm}^{-3}$) at ~ 120 -km altitudes in the deep nightside ionosphere, suggesting enhanced impact ionization by precipitating energetic particles (e.g., Guo, Zeitlin, et al., 2018; Norman et al., 2014; Withers, 2011). Associated with high SEP fluxes, MARSIS also observed the disappearance of ground reflection due to radio wave attenuation (i.e., radio blackout periods) by enhanced ionization below the peak density altitude of $\sim 100\text{--}150$ km (Fowler et al., 2015; Girazian et al., 2017).

During the period of high SEP activity, SEPs penetrated deep into the atmosphere to produce a bright diffuse aurora caused by global precipitation of energetic particles (Schneider et al., 2018). The diffuse aurora was captured in spectral images taken in the mid-UV range (195–220 nm) by MAVEN/IUVS during multiple apoapse orbit segments on 13 September 2017. By mapping the spectral images onto a Mars geographic coordinate system, Schneider et al. (2018) constructed the first complete image of the diffuse aurora at Mars showing a fairly uniform emission enhancement across the observable nightside disk. Compared to the diffuse aurora event reported previously (Jakosky et al., 2015), the emission from this event was 25 times brighter. Based on the IUVS limb scans, these emissions originated from ~ 70 -km altitude.

In the first report of a diffuse aurora, Schneider et al. (2015) found a correlation between the auroral emission and SEP electron events. The peak brightness observed at $\sim 60\text{--}70$ km suggested an association with 100-keV SEP electrons penetrating down to this altitude range in the Martian atmosphere to excite auroral emission. For the September 2017 event, Figure 3e shows the IUVS auroral emission (black circles) overplotted with the 20- to 200-keV SEP electron fluxes. It can be seen that there is no clear distinction for a SEP electron or proton source of this auroral emission (Schneider et al., 2018).

In addition to the observation of a diffuse aurora associated with the SEP activity, Schneider et al. (2018) also reported the detection of discrete auroral emission features that occurred for a short interval on 14 September 2017. From a sequence of IUVS spectral image swaths mapped onto the Mars geographic coordinate system, Schneider et al. (2018) constructed an image of the discrete aurora over the visible nightside disk, which showed the emissions appearing as bright localized patches and curved “wisp” shapes. Overplotting these features onto a statistical map of open and closed magnetic field line topology, they found that the discrete auroral emission features occurred in or near regions with high probability of open magnetic field topology. However, it is currently unclear whether the source of these emissions are due to low-energy electrons accelerated locally in crustal fields, or due to the focusing of high-energy SEPs by the crustal magnetic fields (Schneider et al., 2018). The occurrence of the discrete aurora during the declining phase of SEP event period (see their Figure 3) is consistent with the correlation previously reported by Brain et al. (2006), that the local conditions favorable for discrete aurora to occur are during the time when the plasma environment as a whole is already disturbed.

4.3. SEPs at the Martian Surface

With no global magnetic field at Mars to deflect the charged particles nor a thick atmosphere to shield against them, SEPs with energies of 150 MeV/nuc and higher can penetrate down to the surface (Guo, Zeitlin, et al., 2018; Hassler et al., 2014). The detection of such an event at Mars is analogous to the ground-level enhancement (GLE) event that occurs at Earth when ground-based instruments detect secondary neutrons caused by high energy protons impacting the top of Earth's atmosphere. Typically, a GLE event is caused by SEPs associated with a solar flare or a strong CME shock formed close to the Sun and is observed when Earth is magnetically connected to either of these acceleration sources located at $\sim W90^\circ$. On 10 September 2017, a GLE event was observed at $\sim 16:15$ UT at Earth, caused by ~ 2 -GeV protons impacting the terrestrial atmosphere (Guo, Dumbovic, et al., 2018).

At Mars a GLE event was also observed. As reported by Zeitlin et al. (2018), Ehresmann et al. (2018), and Guo, Dumbovic, et al. (2018), MSL/RAD observed enhancements in the surface radiation dose rates and particles fluxes beginning at 19:50 UT on 10 September 2017, making this event the first simultaneous GLE observation at two planets. Located at the Gale Crater, MSL/RAD has been continuously measuring the radiation environment at the surface since 2012 (Hassler et al., 2014). The source of the radiation is predominantly galactic cosmic rays (GCRs) and occasionally SEPs penetrating down to the surface. During the SEP event, RAD detected an increase above the GCR-induced background levels in the surface proton environment by factors up to 30 for <100 -MeV protons and factors up to 4 for >135 -MeV protons, in addition to the increase in the surface ^4He flux (below 100 MeV nuc^{-1}) by a factor of 10 (Ehresmann et al., 2018). Considering that protons lose roughly 150 MeV of energy passing through the Martian atmosphere, the detection of <100 -MeV SEP protons at the surface by MSL/RAD is consistent with observations of the 80-220 MeV protons by MAVEN/SEP in orbit (i.e., Figure 3c).

For the surface dose rates, MSL/RAD observed factors of 2–3 increase above the GCR-induced background levels (Zeitlin et al., 2018). In terms of the radiation hazards posed by SEPs, the integrated dose over a 30-day interval including the SEP period was well below the NASA exposure limits for astronauts (Zeitlin et al., 2018). Figure 3m shows the measured dose rates from the MSL/RAD-E (plastic) detector. As described by Zeitlin et al. (2018), for SEPs to go through the atmosphere and deposit energy onto MSL/RAD-E, SEP ions with incident energy of at least 275 MeV nuc^{-1} are required. Thus, SEP protons at these energies travel faster such that the rise and peak of the MSL/RAD-E dose rate enhancements is seen to occur earlier than the rise and peak of the MAVEN/SEP-FTO 80- to 220-MeV proton measurements that are shown in Figure 3c.

5. Response of Mars to the ICME Impact

The solar wind have been continuously monitored by MEX since 2004 (Ramstad et al., 2015) and MAVEN since 2014 (Halekas et al., 2017; Lee et al., 2017). Figures 3f–3i show the values observed away from the Martian bow shock and averaged over an orbit for the solar wind speed, density, dynamic pressure, and total magnetic field during 9 September to 18 September 2017 by MEX (blue filled circles) and MAVEN (red filled circles). The MAVEN solar wind parameters were derived from the Solar Wind Ion Analyzer (SWIA; Halekas et al., 2015) and Magnetometer (MAG; Connerney et al., 2015) measurements based on the methodology described in section 3 of Halekas et al. (2017). Figure 4 illustrates the MEX and MAVEN orbit tracks, which are color coded (light to dark) to represent time (earlier to later). The MEX apoapsis segment was positioned well upstream to measure the solar wind. Meanwhile, as the MAVEN orbit precessed its apoapsis location approached near the dusk-dawn terminator within the nominal bow shock location (outer solid line in Figure 4a). Therefore, MAVEN was only occasionally exposed to the solar wind. To provide a more complete MAVEN data set, included in Figures 3f–3g are the solar wind speeds and densities estimated from the SWIA penetrating proton measurements made over an altitude range of 150–250 km (see section 3.2 in Halekas et al., 2017). The proxy data (red open squares) are merged with the upstream measurements (filled circles) to a common 2-hr grid using a simple nearest-neighbor interpolation.

Prior to the solar eruptive activity, both missions were measuring relatively quiet conditions, where the solar wind speed was below 400 km/s and dynamic pressure at 1 nPa. The conditions were moderately disturbed starting on 10 September 2017, when fluctuations in the solar wind densities were observed including the passage of a moderately fast solar wind stream and the related stream interaction region (SIR). The source of this stream is likely the low-latitude to midlatitude coronal hole imaged by STA/EUVI in Figure 1b. Starting at 23:30 UT on 10 September 2017 (after the vertical blue line, "E"), the solar wind density, dynamic pressure, and

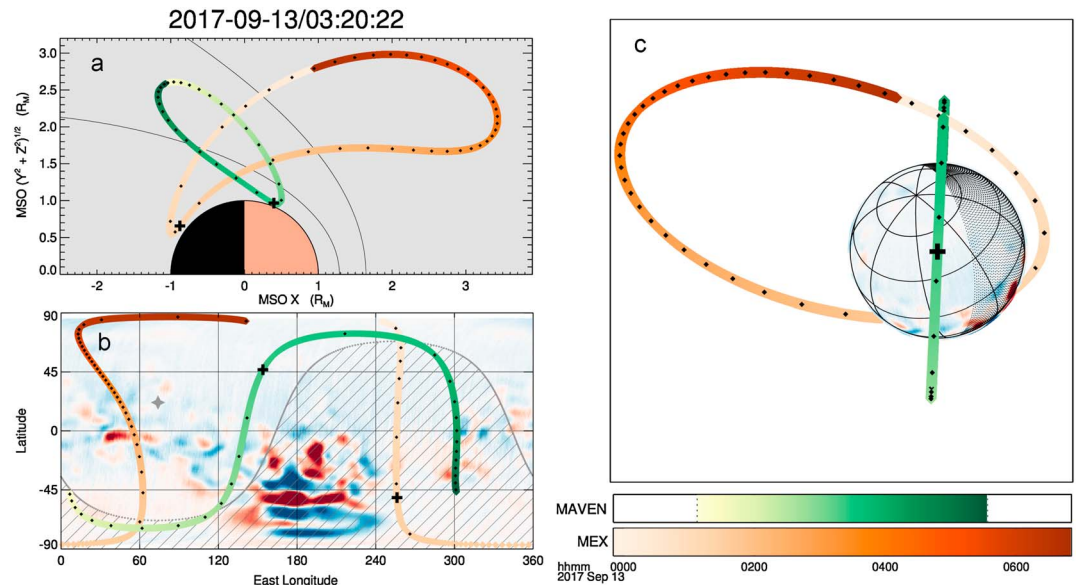


Figure 4. Orbit geometries for MAVEN (green track) and MEX (orange track), color-coded by time. (a) Orbital paths are shown in cylindrical coordinates. The inner line is the average location of the magnetic pileup boundary while the outer line is the average location of the bow shock (Trotignon et al., 2006). (b) Orbits projected onto the radial component of crustal magnetic field at 400 km as determined by Connerney et al. (2002). The dayside and nightside (shaded region) are separated by the terminator (curved black line) at the time of periapsis. The “+” symbol marks the MAVEN and MEX periapsis locations. (c) View of Mars from above the MAVEN periapsis location, with the two spacecraft trajectories, crustal fields and shaded nightside.

interplanetary magnetic field (IMF) magnitude were higher (8 cm^{-3} , 2 nPa , 13 nT ; the peak values were likely higher but not observed) followed by an increase in the solar wind speed ($\sim 530 \text{ km/s}$).

During the ICME event interval, the observation coverage above the bow shock was limited for MEX due to power restrictions. Meanwhile, MAVEN was located within the nominal bow shock location and thus only the penetrating proton proxy estimates for the solar wind density and speed are available. Thus for additional context, the model results from WSA-Enlil are also plotted in Figures 3f–3i (black line). The modeled ICME arrived at $\sim 4:00 \text{ UT}$ on 13 September 2017, with peaks in the modeled speed, density, dynamic pressure, and total IMF (820 km/s , 3.2 cc^{-1} , 3.4 nPa , and 3.8 nT). The overall consistency of the modeled shock arrival time and peak values with the observations gives us confidence in using the WSA-Enlil simulation results together with observations for determining the ICME impact scenario at Mars. From Figure 2f, it is suggested that the ICME made a direct impact at Mars as oppose to a glancing blow, as was the case for Earth. This scenario is also suggested by observations. In Figures 3b–3c, two consecutive brief dropouts are seen in the penetrating particle and SEP observations during the ICME interval. These features, highlighted in gray, appear most prominently in the MAVEN/SWEA observations (Figure 3b) and MAVEN/SEP-FTO observations (Figure 3c). Such a “bite-out” is likely caused by the passage of the magnetic obstacle formed by the merged CMEs (Figures 2c and 2d), suggesting that Mars intersected the ICME structure more centrally (Figure 2f).

A $>20\%$ decrease in the surface radiation dose rates was measured by MSL/RAD during the ICME event (Guo, Dumbovic et al., 2018). Figure 3m shows that the onset of the decrease began at $\sim 2:52 \text{ UT}$ on 13 September 2017, during the time of the observed ICME shock impact (black vertical line, “S”) and that the deepest decrease in dose rate occurred during the encounter of the ICME magnetic obstacle with Mars (interval shaded in gray). The decrease in the dose rate is due to the shock and/or ICME magnetic obstacle acting as a magnetic barrier for the charged particles (e.g., GCRs) to reach the surface. Such an event at Mars is equivalent to the so-called Forbush decrease detected by neutron monitors at Earth (Cane, 2000). Compared to the Forbush decrease events observed previously at Mars, (e.g., Guo, Lillis, et al., 2018; Witasse et al., 2017), the 13 September 2017 event is the deepest one observed to date by MSL/RAD.

The response of the local magnetic topology to the ICME impact is investigated by Xu, Fang, et al. (2018), using MAVEN/SWEA and MAG together with MHD modeling results (e.g., Ma et al., 2018). Understanding the changing magnetic topology (closed, open, or draped magnetic field configuration) driven by variable solar

wind conditions has important implications for energetic particle precipitation patterns in the atmosphere and also for mechanisms that control low energy “cold” ion escape (e.g., ion trapped by closed field lines, polar wind-like ionospheric outflow from below 160–200 km along open field lines connected to the solar wind, and ions stripped away by draped fields via the $j \times B$ force). Figure 3j shows the magnetic topology for draped, open and closed field lines (blue, green, and red, respectively), where each vertical segment represents observations during a MAVEN orbit versus altitude.

The deepest draped field penetration was observed after the ICME shock arrival (blue vertical segment coinciding with the black vertical line marked “S” in Figure 3j). With the enhanced dynamic pressure from the ICME encounter, the draped IMF penetrated down to 200 km into the Martian atmosphere over the northern hemisphere. From the MHD results, Xu, Fang, et al. (2018) also found that more open field lines occurred over the southern hemisphere (see Figures 4b and 4d of Xu, Fang, et al., 2018). These results suggest enhanced cold ion escape occurs at lower altitudes where the ion densities are higher (Xu, Fang, et al., 2018). This disturbed magnetospheric configuration lasted for about 2 days. In addition to the ICME interval, Xu, Fang, et al. (2018) also reported that during the SIR encounter (\sim 2:34 UT on 11 September 2017) the draped IMF extended down to an altitude of \sim 300 km.

From Harada et al. (2018), the low altitude ($<$ 1,000 km) magnetic field magnitude that was directly measured by MAVEN and deduced by MEX/MARSIS showed a significant enhancement over a wide range of solar zenith angles (SZAs). This is presumably caused by the high solar wind dynamic pressure during the ICME encounter. From a comparison of these measurements with Mars Global Surveyor observations, Harada et al. (2018) suggested that the September 2017 ICME event can be classified as a very high dynamic pressure event but weaker than the Halloween 2003 event (Crider et al., 2005).

6. Implications for Atmospheric Escape

The flare, CME, and SEP events reported here provide an opportunity to examine the impact on atmospheric escape. Modeling studies (e.g., Dong et al., 2015; Harnett & Wingless, 2006; Ma & Nagy, 2007) have suggested that atmospheric escape rates increase during time periods of disturbed solar wind. Observational studies (e.g., Edberg et al., 2010; Futaana et al., 2008; Jakosky et al., 2015; Ramstad et al., 2017) generally support this idea, though evaluating global escape rates during such periods is hampered in at least two ways. First, such events have sufficiently short duration that a spacecraft at a given location cannot sample all relevant escape channels from Mars. Second, increased fluxes of SEPs can lead to increased instrument background levels. Disturbed time periods also provide a foothold for evaluating atmospheric escape at earlier epochs in Mars history, since the solar and solar wind inputs during such time periods are likely to have been more intense than the current quiescent conditions (e.g., Ribas et al., 2005; Wood et al., 2005).

Atmospheric escape at Mars (or any planet) proceeds through a variety of physical mechanisms, each of which results in providing upper atmospheric particles with sufficient energy to escape the planet. Measurements from MAVEN during the event, as well as models of the event time period, have enabled estimates of the change in escape rates for most of these processes.

The escape of hydrogen from Mars is dominated by thermal escape, and estimates of the rate of loss typically require knowledge of densities and temperatures in the exobase region. Mayyasi et al. (2018) used in situ measurements of CO₂ and Ar densities from MAVEN/NGIMS to constrain the neutral upper atmospheric temperatures and observations of hydrogen Lyman- α emission intensities by MAVEN/IUVS are fit to a spherically symmetric radiative transfer model for the upper atmosphere to derive the exobase density. This model was then used to estimate the hydrogen thermal escape rate. Driven by an increase in the exobase temperature of hydrogen, the escape rates increased by a factor of \sim 5 during the event.

In regard to oxygen, these atoms are too massive to escape thermally from Mars in any significant amount, and instead escape largely by photochemical processes whereby molecular oxygen ions dissociatively recombine. The response of the Martian ionosphere to the X8.2 flare was explored by Thiemann et al. (2018), who used MAVEN measurements of T_e , abundances of O₂⁺, and atmospheric neutral densities to estimate photochemical escape rates using the model of Lillis et al. (2017). They found a noticeable (\sim 50%) increase in oxygen escape during a single orbit (\sim 4.5 hr) following the flare. This increase in photochemical escape was also inferred from coupled global simulations by Lee et al. (2018) of the Martian exosphere, thermosphere, and plasma environment for time periods encompassing the flare. They found an increase of \sim 20% in the escape

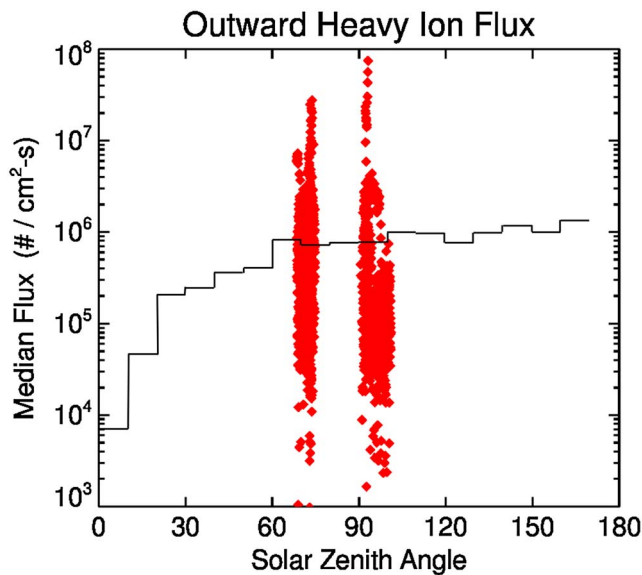


Figure 5. Comparison of outward-directed planetary heavy ion fluxes measured by MAVEN from 10 September 2017 through 18 September 2017 (red symbols) to the median outward directed fluxes measured by MAVEN from November 2014 through September 2016 (black line as a function of SZA). All observations were taken from a 1.25–1.45 R_M spherical shell around Mars.

rate shortly following the flare, and a rapid decrease within ~ 2.5 hr followed by a gradual return to nominal escape conditions.

Measurements of planetary ion escape are continuously made by MAVEN and have been evaluated based on the fluxes of heavy ions measured in a spherical shell with thickness of $0.2 R_M$ and centered around Mars at $1.35 R_M$ ($\sim 1,200$ -km altitudes; Brain et al., 2015). Figure 5 shows the comparison of the outward-directed planetary heavy ion fluxes measured between 10 September 2017 through 18 September 2017 with the median outward ion fluxes at similar SZAs recorded over many months. In general, the observed escaping fluxes during the event are lower than those typically recorded by MAVEN. However, there are a few brief time periods, particularly after the ICME arrival, where instantaneous escaping fluxes are enhanced by a factor of ~ 40 . Integrated over the entire event period from flare arrival until after the ICME passage, the average escaping flux is enhanced by a factor of ~ 2 . We further note that the limited MAVEN orbital coverage during the event prevents a true assessment of the global change in ion escape rates because other regions could have experienced different magnitudes of enhancement in escaping fluxes. We take these results as indicating that escape fluxes increased in at least some locations, and may have increased globally.

A global picture of ion escape during the event period is, however, made possible using simulations validated by observations. The CME event was simulated by Ma et al. (2018) using an MHD model and by Romanelli et al.

(2018) using a hybrid model. Both global plasma models were driven with MAVEN and proxy measurements of the solar EUV photon flux, solar wind, and IMF at Mars. Ma et al. (2018) used the MHD model to run both steady-state and time-dependent simulations, and showed increases in heavy ion escape of a factor of 10–20, with rates as high as $\sim 3 \times 10^{25} \text{ s}^{-1}$ for at least ~ 5 hr, in excess of those reported by Lee et al. (2018) for photochemical escape using the same model framework. Both models showed good agreement with quantities measured by MAVEN along its orbit, such as magnetic field strength and direction, plasma velocity, and plasma density. This agreement gives confidence to the ability of the models to estimate ion escape rates. Romanelli et al. (2018) ran the hybrid model for three steady-state cases corresponding to three different time periods encompassing the CME event. They found that the escape fluxes of O^+ were enhanced by a factor of 2.5 during the event—much less than the enhancement obtained from the MHD model. In addition, they found that the escape of H^+ (not simulated by the MHD model) increased by a factor of ~ 10 , to $\sim 2 \times 10^{26} \text{ s}^{-1}$. We note that this rate is roughly comparable to thermal escape rates for neutral hydrogen that were reported by Mayyasi et al. (2018).

7. Concluding Remarks

The 10 September 2017 solar eruptive event provided an opportunity for instruments on board MAVEN, MEX, and MSL, to simultaneously observe the space weather impact at Mars. The timeline of the events summarized in this overview is presented in Table 1. The response of Mars to the solar events included the heating of the atmosphere by an X-class flare, global auroral emissions due to particle precipitation related to the high influx of SEPs, dramatic changes in the surface radiation environment due to high energy SEP protons, deep penetration of magnetosheath fields upon the ICME impact, and indications of enhanced planetary ion escape.

While solar flares and CME eruptions occur throughout the solar cycle, such relatively rare strong events have not been previously observed in such detail at Mars. The availability of supporting observations from other heliospheric vantage points and contextual information from global solar corona-solar wind modeling results also increases the scientific value of this event. One other event that greatly impacted Mars and Earth was the well-known Halloween Storm of 2003 (Crider et al., 2005; Gopalswamy et al., 2005). However, only limited observations were available for interpretation of the Mars response. In addition, the September 2017 event

Table 1
Timeline of Events at Mars During the September 2017 Solar Events Period

| Date | Time (UT) | Event description | Mission/ Instrument | Related references | |
|--------------|-----------------------|--|---------------------------------------|--|------------|
| 10 September | 15:40:30 | Start of X8.2 flare in 0- to 7-nm solar irradiance | MAVEN/EUVM | Chamberlin et al. (2018) | |
| | 15:54:00 | Detection of solar hard X-rays from X8.2 flare | MAVEN/SEP | This study | |
| | 15:54:34 | CME eruption | SDO/AIA | Guo, Dumbovic, et al. (2018) | |
| | 16:00:00 | First appearance of CME in coronagraph FOV | SOHO/LASCO C2 | | |
| | 16:02:00 | Peak of X8.2 flare in Lyman- α | MAVEN/EUVM | Chamberlin et al. (2018) | |
| | 16:03:40 | 80% enhancement in ionizing EUV irradiance | MAVEN/EUVM | Thiemann et al. (2018) | |
| | 16:11:30 | Peak of X8.2 in 0- to 7-nm solar irradiance | MAVEN/EUVM | Chamberlin et al. (2018) | |
| | 17:30:41 ^a | Expansion of neutral atmosphere from flare heating | MAVEN/NGIMS | Elrod et al. (2018) | |
| | 17:35:56 ^a | 70 K increase in thermospheric temperature | MAVEN/IUVS | Jain et al. (2018) | |
| | 19:20:00 | Arrival of 20- to 200-keV SEP electrons | MAVEN/SEP | This study | |
| | 19:50:00 | Rise in surface radiation above background level and arrival of >275-MeV/nuc ion | MSL/RAD | Zeitlin et al. (2018) Guo, Dumbovic, et al. (2018) Ehresmann et al. (2018) | |
| | | 22:00:00 | Arrival of 80- to 220-MeV SEP protons | MAVEN/SEP | This study |
| | | | Arrival of 15- to 100-MeV SEP protons | MAVEN/SEP | This study |
| | | | Rise in penetrating background counts | MAVEN/SWEA | This study |
| | 23:30:00 | Impact by an SIR | MAVEN/SWIA & MAG MEX/ASPERA-3 | This study | |
| | 23:38:04 ^b | Rise in penetrating background counts rate | MEX/ASPERA-3 | Ramstad et al. (2018) | |
| 11 September | 2:34:00 | IMF draping down to 300 km due to SIR | MAVEN/SWEA, MAG | Xu, Fang, et al. (2018) | |
| | 6:30:00 | Peak in proton fluxes at the surface | MSL/RAD | Ehresmann et al. (2018) | |
| | | Peak in surface dose rate | | Zeitlin et al. (2018) | |
| | 18:52:30 | Peak in 80- to 220-MeV SEP protons | MAVEN/SEP | This study | |
| 12 September | 17:57:30 | Peak in 15- to 100-MeV SEP protons | MAVEN/SEP | This study | |
| 13 September | 2:30:00 | Peak emission of diffuse aurora | MAVEN/IUVS | Schneider et al. (2018) | |
| | 2:52:13 | ESP enhancement due to ICME shock arrival | MAVEN/SWEA, SEP | This study | |
| | | Onset of Forbush decrease | MSL/RAD | Guo, Dumbovic, et al. (2018) | |
| | | IMF draping down to 200 km due to ICME | MAVEN/SWEA, MAG | Xu, Fang, et al. (2018) | |
| | 5:40:00 | SEP bite-out from ICME magnetic obstacle | MAVEN/SWEA, SEP | This study | |

Note. CME = coronal mass ejection; ICME = interplanetary coronal mass ejection; MSL = Mars Science Laboratory; SEP = solar energetic particle; RAD = Radiation Assessment Detector; SWEA = Solar Wind Electron Analyzer; MAG = magnetometer; MEX = Mars Express; SOHO = Solar and Heliospheric Observatory; LASCO = Large Angle and Spectrometric Coronagraph; AIA = Atmospheric Imaging Assembly; FOV = field of view; MAVEN = Mars Atmosphere and Volatile Evolution.

^a Closest time available from MAVEN periapsis measurements. ^b Time after observational data gap.

observations at Mars are particularly valuable for providing a different solar and heliospheric perspective of space weather consequences. For example, Luhmann et al. (2018) used MAVEN/SEP proton observations to establish the heliospheric scenario for the widespread SEP occurrence during the event period.

However, perhaps of most importance are the potential implications of these observations at Mars for what they may tell us about how a terrestrial planet other than Earth with its own distinctive characteristics of size, atmosphere, planetary magnetic field and heliocentric distance responds to strong solar activity. The combination of phenomena observed at Mars (e.g., transient flare heating and added ionization of neutrals, enhanced atmospheric ion pickup followed by precipitation or escape, SEP energy deposition-related atmospheric emissions) reveal both Earth-like and distinctly Martian responses during space weather storms. In addition, these observations reinforce the idea that space weather events have had impacts throughout the history of Mars and more broadly the solar system that cannot be ignored in the big-picture reconstructions of their evolution.

Acknowledgments

The MAVEN mission has been made possible through NASA sponsorship and the dedicated efforts of NASA Goddard Space Flight Center, LASP, Lockheed Martin, and the MAVEN Technical and Science Teams. The interpretation of the MAVEN observations described here benefited from the earlier observations and analyses of space weather events on MEX, which provided some examples of events from the more active preceding solar cycle. The MAVEN and MSL data shown are publicly available at the NASA Planetary Data System website (<http://ppi.pds.nasa.gov>). The MEX ASPERA-3 data are available at the ESA Planetary Science Archive. The GOES-13 data are available at the NOAA National Centers for Environmental Information website (<https://www.ngdc.noaa.gov/>). The WSA-Enlil simulation results (run name "Leila_Mays_120817_SH_9", made by special request) were provided by the NASA/GSFC Community Coordinated Modeling Center through their public Runs on Request system (<http://ccmc.gsfc.nasa.gov>). We also acknowledge using solar observations from SOHO/LASCO, SDO/AIA, STA/EUVI and STA/SECCHI, and in situ measurements from STA/HET. We would like to thank E. Thiemann, A. Rahmati, R. Lillis, P. Dunn, B. Ehresmann, J. Gruesbeck, P. Chamberlin, S. Xu, R. Ramstad, T. Hara, J. McFadden, C. Fowler, L. Andersson, J. Espley, A. Poppe, S. Curry, M. Elrod, S. Jain, and N. Schneider for their helpful insights and discussions.

References

- Andersson, L., Ergun, R. E., Delory, G. T., Ericsson, A., Westfall, J., Reed, H., et al. (2015). The Langmuir Probe and Waves (LPW) Instrument for MAVEN. *Space Science Reviews*, *195*, 173–198.
- Arge, C. N., Luhmann, J. G., Odstrcil, D., Schrijver, C. J., & Li, Y. (2004). Stream structure and coronal sources of the solar wind during the May 12th, 1997 CME. *Journal of Atmospheric and Solar - Terrestrial Physics*, *66*, 1295–1309.
- Aschwanden, M. J. (1994). Irradiance observations of the 1–8 Å solar soft X-ray flux from GOES. *Solar Physics*, *152*, 53–59.
- Brain, D. A., Halekas, J. S., Peticolas, L. M., Lin, R. P., Luhmann, J. G., Mitchell, D. L., et al. (2006). On the origin of aurorae on Mars. *Geophysical Research Letters*, *33*, L01201. <https://doi.org/10.1029/2005GL024782>
- Brain, D. A., McFadden, J. P., Halekas, J. S., Connerney, J. E. P., Bougher, S. W., Curry, S., et al. (2015). The spatial distribution of planetary ion fluxes near Mars observed by MAVEN. *Geophysical Research Letters*, *41*, 9142–9148. <https://doi.org/10.1002/2015GL065293>
- Brueckner, G. E., Howard, R. A., Koomen, M. J., Korendyke, C. M., Michels, D. J., Moses, J. D., et al. (1995). The Large Angle Spectroscopic Coronagraph (LASCO). *Solar Physics*, *162*, 357–402.
- Cane, H. V. (2000). Coronal mass ejections and Forbush decreases. *Space Science Reviews*, *93*, 55–77.
- Capalbo, F. J. (2010). Background analysis for IMA sensor on ASPERA instrument (IRF Technical Report 54). Kiruna, Sweden: Swedish Institute of Space Physics.
- Chamberlin, P. C., Woods, T. N., Didkovsky, L., Eparvier, F. G., Jones, A. R., Mason, J. P., et al. (2018). Solar ultraviolet irradiance observations of the solar flares during the intense September 2017 storm period. *Space Weather*. <https://doi.org/10.1029/2018SW001866>
- Connerney, J. E. P., Espley, J., Lawton, P., Murphy, S., Odom, J., Oliverson, R., & Sheppard, D. (2015). The MAVEN magnetic field investigation. *Space Science Reviews*, *195*, 257–291. <https://doi.org/10.1007/s11214-015-0169-4>
- Crider, D. H., Espley, J., Brain, D. A., Mitchell, D. L., Connerney, J. E. P., & Acuna, M. (2005). Mars Global Surveyor observations of the Halloween 2003 solar superstorm's encounter with Mars. *Journal of Geophysical Research*, *110*, A09S21. <https://doi.org/10.1029/2001JA010881>
- Dong, C., Ma, Y., Bougher, S. W., Toth, G., Nagy, A. F., Halekas, J. S., et al. (2015). Multifluid MHD study of the solar wind interaction with Mars' upper atmosphere during the 2015 March 8th ICME event. *Geophysical Research Letters*, *42*, 9103–9112. <https://doi.org/10.1002/2015GL065944>
- Edberg, N. J. T., Nilsson, H., Williams, A. O., Lester, M., Milan, S. E., Cowley, S. W. H., et al. (2010). Pumping out the atmosphere of Mars through solar wind pressure pulses. *Geophysical Research Letters*, *37*, L03107. <https://doi.org/10.1029/2009GL041814>
- Ehresmann, B., Hassler, D. M., Zeitlin, C. J., Guo, J., Wimmer-Schweingruber, R. F., Matthiä, D., et al. (2018). Energetic particle radiation environment observed by RAD on the surface of Mars during the September 2017 event. *Geophysical Research Letters*, *45*, 5305–5311. <https://doi.org/10.1029/2018GL077801>
- Elrod, M. K., Curry, S. M., Thiemann, E. M. B., & Jain, S. K. (2018). September 2017 solar flare event: Rapid heating of the Martian neutral exosphere from the X-class flare as observed by MAVEN. *Geophysical Research Letters*, *45*. <https://doi.org/10.1029/2018GL077729>
- Eparvier, F. G., Chamberlin, P. C., Woods, T. N., & Thiemann, E. M. B. (2015). The Solar Extreme Ultraviolet Monitor for MAVEN. *Space Science Reviews*, *195*, 293–301.
- Fowler, C. M., Andersson, L., Ergun, R. E., Morooka, M., Delory, G., Andrews, D. J., et al. (2015). The first in situ electron temperature and density measurements of the Martian nightside ionosphere. *Geophysical Research Letters*, *42*, 8854–8861. <https://doi.org/10.1002/2015GL065267>
- Futaana, Y., Barabash, S., Yamauchi, M., McKenna-Lawlor, S., Lundin, R., Luhmann, J. G., et al. (2008). Mars express and Venus express multi-point observations of geoeffective solar flare events in December 2006. *Planetary and Space Science*, *56*, 873.
- Girazian, Z., Mahaffy, P., Lillis, R. J., Benna, M., Elrod, M., Fowler, C. M., & Mitchell, D. L. (2017). Ion densities in the nightside ionosphere of Mars: Effects of electron impact ionization. *Geophysical Research Letters*, *44*, 11,248–11,256. <https://doi.org/10.1002/2017GL075431>
- Gopalswamy, N., Yashiro, S., Liu, Y., Michalek, G., Vourlidas, A., Kaiser, M. L., & Howard, R. A. (2005). Coronal mass ejections and other extreme characteristics of the 2003 October–November solar eruptions. *Journal of Geophysical Research*, *110*, A09S15. <https://doi.org/10.1029/2004JA010958>
- Guo, J., Dumbovic, M., Wimmer-Schweingruber, R. F., Temmer, M., Lohf, H., Wang, Y., et al. (2018). Modeling the evolution and propagation of the 2017 September 9th and 10th CMEs and SEPs arriving at Mars constrained by remote-sensing and in-situ measurement. *Space Weather*. <https://doi.org/10.1029/2018SW001973>
- Guo, J., Lillis, R., Wimmer-Schweingruber, R. F., Zeitlin, C., Simonson, P., Rahmati, A., et al. (2018). Measurements of Forbush decreases at Mars: both by MSL on ground and by MAVEN in orbit. *Astronomy and Astrophysics*, *611*, A79. <https://doi.org/10.1051/0004-6361/201732087>
- Guo, J., Zeitlin, C., Wimmer-Schweingruber, R. F., McDole, T., Kuhl, P., Appel, J. C., et al. (2018). A generalized approach to model the spectra and radiation dose rate of solar particle events on the surface of Mars. *Astronomy Journal*, *155*(49). <https://doi.org/110.3847/1538-3881/aaa085>
- Gurnett, D., Huff, R., Morgan, D., Persoon, A., Averkamp, T., Kirchner, D., et al. (2008). An overview of radar soundings of the martian ionosphere from the Mars Express spacecraft. *Advances in Space Research*, *41*(9), 1335–1346. <https://doi.org/10.1016/j.asr.2007.01.062>
- Gurnett, D. A., Kirchner, D. L., Huff, R. L., Morgan, D. D., Persoon, A. M., Averkamp, T. F., et al. (2005). Radar soundings of the ionosphere of Mars. *Science*, *310*, 1929–1933. <https://doi.org/10.1126/science.1121868>
- Halekas, J. S., Ruhunusiri, S., Harada, Y., Collinson, G., Mitchell, D. L., Mazelle, C., et al. (2017). Structure, dynamics, and seasonal variability of the mars-solar wind interaction: MAVEN solar wind ion analyzer inflight performances and science results. *Journal of Geophysical Research: Space Physics*, *122*, 547–578. <https://doi.org/10.1002/2016JA023167>
- Halekas, J. S., Taylor, E. R., Dalton, G., Johnson, G., Curtis, D. W., McFadden, J. P., et al. (2015). The Solar Wind Ion Analyzer for MAVEN. *Space Science Reviews*, *195*, 125–151.
- Harada, Y., Gurnett, D. A., Kopf, A. J., Halekas, J. S., Ruhunusiri, S., DiBraccio, G. A., et al. (2018). MARSIS observations of the Martian nightside ionosphere during the September 2017 solar event. *Geophysical Research Letters*, *45*. <https://doi.org/10.1002/2018GL077622>
- Harnett, E. M., & Winglee, R. M. (2006). Three-dimensional multifluid simulations of ionospheric loss at Mars from nominal solar wind conditions to magnetic cloud events. *Journal of Geophysical Research*, *111*, A09213. <https://doi.org/10.1029/2006JA011724>
- Hassler, D. M., Zeitlin, C., Wimmer-Schweingruber, R. F., Bottcher, S., Martin, C., Andrews, J., et al. (2012). The radiation assessment detector (RAD) investigation. *Space Science Reviews*, *170*, 503–558. <https://doi.org/10.1007/s11214-012-9913-1>
- Hassler, D. M., Zeitlin, C., Wimmer-Schweingruber, R. F., Ehresmann, B., Rafkin, S., Eigenbrode, J. L., et al. (2014). Mars' surface radiation environment measured with the Mars science laboratory's Curiosity Rover. *Science*, *343*, 1244797. <https://doi.org/10.1126/science.1244797>
- Jain, S., Deighan, J., Schneider, N. M., Stewart, A. I. F., Evans, J. S., Thiemann, E. M. B., et al. (2018). Response of Martian thermosphere to the X8.2 solar flare of 10 September 2017 as seen by MAVEN/IUVS. *Geophysical Research Letters*, *45*. <https://doi.org/10.1029/2018GL077731>
- Jakosky, B. M., Grebowsky, J. M., Luhmann, J. G., Connerney, J., Eparvier, F., Ergun, R., et al. (2015). MAVEN observations of the response of Mars to an interplanetary coronal mass ejection from the Sun. *Science*, *350*, aad0210. <https://doi.org/10.1126/science.aad0210>

- Kaiser, M. (2005). The STEREO mission: An overview. *Advances in Space Research*, 36, 1483–1488.
- Larson, D. E., Lillis, R. J., Lee, C. O., Hatch, K., Robinson, M., Glaser, D., Chen, J., et al. (2015). The MAVEN solar energetic particle investigation. *Space Science Reviews*, 195, 153–172.
- Lee, C. O., Arge, C. N., Odstrcil, D., Millward, G., Pizzo, V., & Lugaz, N. (2015). Ensemble modeling of successive halo CMEs: A case study. *Solar Physics*, 290, 1207–1229. <https://doi.org/10.1007/s11207-015-0667-2>
- Lee, C. O., Arge, C. N., Odstrcil, D., Millward, G., Pizzo, V., Quinn, J. M., & Henney, C. J. (2013). Ensemble modeling of CME propagation. *Solar Physics*, 285, 349–368. <https://doi.org/10.1029/2011SW000748>
- Lee, Y., Dong, C., Pawlowski, D., Thiemann, E., Tenishev, V., Mahaffy, P., et al. (2018). Effects of a solar flare on the Martian hot O corona and photochemical escape. *Geophysical Research Letters*, 45(14), 6814–6822. <https://doi.org/10.1029/2018GL077732>
- Lee, C. O., Hara, T., Halekas, J. S., Thiemann, E., Chamberlin, P., Eparvier, F., et al. (2017). MAVEN observations of the solar cycle 24 space weather conditions at Mars. *Journal of Geophysical Research: Space Physics*, 122, 2768–2794. <https://doi.org/10.1002/2016JA023495>
- Lemen, J. R., Title, A. M., Akin, D. J., Boerner, P. F., Chou, C., Drake, J. F., et al. (2012). *The atmospheric imaging assembly (AIA) on the solar dynamics observatory (SDO)*, vol. 275, pp. 17–40. <https://doi.org/10.1007/s11207-011-9776-8>
- Lillis, R. J., Lee, C. O., Larson, D. E., Luhmann, J. G., Halekas, J. S., Connerney, J. E. P., & Jakosky, B. M. (2017). Photochemical escape of oxygen from Mars: First results from MAVEN in situ data. *Journal of Geophysical Research: Space Physics*, 122, 3815–3836. <https://doi.org/10.1002/2016JA023525>
- Lollo, A., Withers, P., Fallows, K., Girazian, Z., Matta, M., & Chamberlin, P. C. (2012). Numerical simulations of the ionosphere of Mars during a solar flare. *Journal of Geophysical Research*, 117, A05314. <https://doi.org/10.1029/2011JA017399>
- Luhmann, J. G., Mays, M. L., Li, Y., Lee, C. O., Bain, H., Odstrcil, D., et al. (2018). Shock connectivity and the late cycle 24 solar energetic particle events in July and September 2017. *Space Weather*, 16, 557–568. <https://doi.org/10.1029/2018SW001860>
- Ma, Y., Fang, X., Halekas, J. S., Xu, S., Russell, C. T., & Luhmann, J. G. (2018). The Impact and solar wind proxy of the 2017 September ICME event at Mars. *Geophysical Research Letters*, 45. <https://doi.org/10.1029/2018GL077707>
- Ma, Y. J., & Nagy, A. F. (2007). Ion escape fluxes from Mars. *Geophysical Research Letters*, 34, L08201. <https://doi.org/10.1029/2006GL029208>
- Mahaffy, P. R., et al. (2015). The Neutral Gas and Ion Mass Spectrometer on the Mars Atmosphere and Volatile Evolution Mission. *Space Science Reviews*, 195, 49–73. <https://doi.org/10.1007/s11214-014-0091-1>
- Mays, M. L., Taktakishvili, A., Pulkkinen, A., MacNeice, P. J., Rastätter, L., Odstrcil, D., et al. (2015). Ensemble modeling of CMEs using the WSA-ENLIL+Cone model. *Solar Physics*, 290, 1775–1814. <https://doi.org/10.1007/s11207-015-0692-1>
- Mayyasi, M., Bhattacharyya, D., Clarke, J., Benna, M., Mahaffy, P., Thiemann, E. M. B., et al. (2018). Significant space weather impact on the escape of hydrogen from Mars. *Geophysical Research Letters*, 45. <https://doi.org/10.1029/2018GL077727>
- Mendillo, M., Klobuchar, J. A., Fritz, R. B., Da Rosa, A. V., Kersley, L., Yeh, K. C., et al. (1974). Behavior of the ionospheric F region during the great solar flare of August 7, 1972. *Journal of Geophysical Research*, 79(4), 665–672.
- Norman, R. B., Gronoff, G., & Mertens, C. J. (2014). Influence of dust loading on atmospheric ionizing radiation on Mars. *Journal of Geophysical Research: Space Physics*, 119, 452–461. <https://doi.org/10.1002/2013JA019351>
- Odstrcil, D. (2003). Modeling 3D solar wind structure. *Advances in Space Research*, 32, 497–506.
- Pesnell, W. D., Thompson, B. J., & Chamberlin, P. C. (2012). The Solar Dynamics Observatory (SDO). *Solar Physics*, 275, 3. <https://doi.org/10.1007/s11207-011-9841-3>
- Ramstad, R., Barabash, S., Futaana, Y., Nilsson, H., Wang, X.-D., & Holmstrom, M. (2015). The Martian atmospheric ion escape rate dependence on solar wind and solar EUV conditions I: Seven years of Mars Express observations. *Journal of Geophysical Research: Planets*, 120, 1298–1309. <https://doi.org/10.1002/2015JE004816>
- Ramstad, R., Barabash, S., Futaana, Y., Yamauchi, M., Nilsson, H., & Holmstrom, M. (2017). Mars under primordial solar wind conditions: Mars express observations of the strongest CME detected at Mars under solar cycle #24 and its impact on atmospheric ion escape. *Geophysical Research Letters*, 44, 10,805–10,811. <https://doi.org/10.1002/2017GL075446>
- Ramstad, R., Holmstrom, M., Futaana, Y., Lee, C. O., Rahmati, A., Dunn, P., et al. (2018). The September 2017 SEP event in context with the current solar cycle: Mars Express ASPERA-3/IMA and MAVEN/SEP observations. *Geophysical Research Letters*, 45. <https://doi.org/10.1029/2018GL077842>
- Ribas, I., Guinan, E. F., Gudel, M., & Audard, M. (2005). Evolution of the Solar activity over time and effects on planetary atmospheres. I. High-energy irradiances (1–1700). *The Astrophysical Journal*, 622(1), 680–694. <https://doi.org/10.1086/427977>
- Romanelli, N., Modolo, R., LeBlanc, F., Chaufray, J.-Y., Martinez, A., Ma, Y., et al. (2018). Responses of the Martian magnetosphere to an interplanetary coronal mass ejection: MAVEN observations and LatHyS results. *Geophysical Research Letters*, 45. <https://doi.org/10.1029/2018GL077714>
- Schneider, N., Deighan, J. I., Jain, S. K., Stiepen, A., Evans, J. S., Stewart, A. I. F., et al. (2015). The discovery of diffuse aurora on Mars. *Science*, 350, aad0313. <https://doi.org/10.1126/science.aad0313>
- Schneider, N., Jain, S. K., Deighan, J. I., Nasr, C. R., Brain, D. A., Larson, D., et al. (2018). Global aurora on Mars during the September 2017 space weather event. *Geophysical Research Letters*, 45. <https://doi.org/10.1029/2018GL077772>
- Thiemann, E. M. B., Andersson, L. A., Lillis, R., Withers, P., Xu, S., Elrod, M., et al. (2018). The Mars upper ionosphere response to the X8.2 solar flare of 10 September 2017. *Geophysical Research Letters*, 45. <https://doi.org/10.1029/2018GL077730>
- Thiemann, E. M. B., Eparvier, F. G., Andersson, L. A., Fowler, C. M., Peterson, W. K., Mahaffy, P. R., & Deighan, J. I. (2015). Neutral density response to solar flares at Mars. *Geophysical Research Letters*, 42, 8986–8992. <https://doi.org/10.1002/2015GL066334>
- Troignon, J. G., Mazelle, C., Bertucci, C., & Acuna, M. H. (2006). Martian shock and magnetic pile-up boundary positions and shapes determined from the Phobos 2 and Mars Global Surveyor data sets. *Planetary and Space Science*, 54(4), 357–369. <https://doi.org/10.1016/j.pss.2006.01.003>
- von Roseninge, T. T., Reames, D. V., Baker, R., Hawk, J., Nolan, J. T., Ryan, L., et al. (2008). The high energy telescope for STEREO. *Space Science Reviews*, 136, 391–335. <https://doi.org/10.1007/s11214-007-9300-5>
- Witasse, O., Sánchez-Cano, B., Mays, M. L., Kajdic, P., Opgenoorth, H., Elliott, H. A., et al. (2017). Interplanetary coronal mass ejection observed at STEREO-A, Mars, comet 67P/Churyumov-Gerasimenko, Saturn, and New Horizons en route to Pluto: Comparison of its Forbush decreases at 1.4, 3.1, and 9.9 AU. *Journal of Geophysical Research: Space Physics*, 122, 7865–7890. <https://doi.org/10.1002/2017JA023884>
- Withers, P. (2011). Attenuation of radio signals by the ionosphere of Mars: Theoretical development and application to MARSIS observations. *Radio Science*, 46, RS2004. <https://doi.org/10.1029/2010RS004450>
- Wood, B. E., Müller, H. R., Zank, G. P., Linsky, J. L., & Redfield, S. (2005). New mass-loss measurements from astrospheric Ly α absorption. *The Astrophysical Journal*, 628(2), L143–L146. <https://doi.org/10.1086/432716>
- Xu, S., Fang, X., Mitchell, D. L., Ma, Y., Luhmann, J. G., DiBraccio, G. A., et al. (2018). Investigation of Martian magnetic topology response to 2017 September ICME. *Geophysical Research Letters*, 45. <https://doi.org/10.1029/2018GL077708>

- Xu, S., Thiemann, E., Mitchell, D. L., Eparvier, F., Pawlowski, D., Benna, M., et al. (2018). Observations and modeling of low-altitude ionospheric responses to 2017 September solar flare at Mars. *Geophysical Research Letters*, 45. <https://doi.org/10.1029/2018GL078524>
- Zeitlin, C., Hassler, D. M., Guo, J., Ehresmann, B., Wimmer-Schweingruber, R. F., Rafkin, S. C. R., et al. (2018). Analysis of the radiation hazard observed by RAD on the surface of Mars during the September 2017 solar particle event. *Geophysical Research Letters*, 45, 5845–5851. <https://doi.org/10.1029/2018GL077760>